PAPER

Highly monodisperse $Cu_3Mo_2O_9$ micropompons with excellent performance in photocatalysis, photocurrent response and lithium storage†

Juan Xia,[a] Le Xin Song,[*ab] Wei Liu,[*a] Yue Teng,[a] Qing Shan Wang,[b] Li Zhao[b] and Mao Mao Ruan[b]

We developed a simple and facile method for preparing two types of transition metal molybdates: $AMoO_4$ (A = Ni and Zn) and $B_3Mo_2O_9$ (B = Cu and Zn). Initially, a hydrothermal reaction at 383 K for 10 h in an aqueous solution of ammonium molybdate tetrahydrate (AMT) and metal acetates (MAc_2, M = Ni, Cu and Zn) was carried out to synthesize their precursors: $NiMoO_4 \cdot xH_2O$, $ZnMoO_4 \cdot 0.8H_2O$, $Cu_3(OH)_2(MoO_4)_2$ and $Zn_3(OH)_2(MoO_4)_2$. Subsequently, $AMoO_4$ with a 1D structure and $B_3Mo_2O_9$ with a 3D structure were successfully constructed by sintering the precursors at 873 K for 3 h in air. Our result presented the first evidence that the generation of α-$ZnMoO_4$ and $Zn_3Mo_2O_9$ is dependent on the initial concentration of AMT or $Zn(Ac)_2$. More importantly, a highly monodisperse $Cu_3Mo_2O_9$ micropompon structure was successfully created by an ethylenediaminetetraacetic acid (H_4Y)-mediated hydrothermal route and a subsequent sintering process. We considered that H_4Y, a strong competitive chelating ligand, played a significant role in prohibiting the formation of the intermediate $(NH_4)_2Cu(MoO_4)_2$, thereby not only producing a monodisperse structure of $Cu_3(OH)_2(MoO_4)_2$ but also reducing the size of the structure by forming a stable complex: CuY. Three independent experiments: photocatalysis, photocurrent response and lithium storage were performed to discuss several possible applications of the as-obtained $Cu_3Mo_2O_9$ micropompons. Our data demonstrated that the $Cu_3Mo_2O_9$ material exhibited excellent photocatalytic efficiency for the degradation of Congo red under visible light irradiation. Also, the time-dependent photoresponse of the $Cu_3Mo_2O_9$ gave a very high ratio (about 171) of light current to dark current and a stable photocurrent density, which were a reflection of a high concentration of photogenerated electron–hole pairs. Further, the material indicated good charge–discharge stability and high coulombic efficiency in lithium-ion batteries even during the 100 cycles. We believe that the present study represents a significant step in the development of transition metal molybdates.

1. Introduction

In the past two decades, much attention has been paid to the structures of transition metal molybdates mainly including

[a]CAS Key Laboratory of Materials for Energy Conversion, Department of Materials Science and Engineering, University of Science and Technology of China, Jin Zhai Road 96, Hefei 230026, P. R. China. E-mail: solexin@ustc.edu.cn; wliu@ustc.edu.cn
[b]Department of Chemistry, University of Science and Technology of China, Jin Zhai Road 96, Hefei 230026, P. R. China

$AMoO_4$ (A = Fe, Co, Ni, Cu and Zn)[1–3] and $B_3Mo_2O_9$ (B = Cu and Zn) types,[4] due to their promising applications in many fields, such as catalysis, luminescence and energy storage.[5–7] Also, there are many studies on the formation of various ordered structures of $AMoO_4$ type by various methods, such as sol-vothermal and hydrothermal synthesis, sintering and chemical vapor deposition.[8] Although the effect of transition metal valence states on the composition of molybdates has been reported by several groups,[9] possible condition-dependent synthesis of different types of transition metal molybdates still has not been experimentally established. Thus, we designed a series experiments using a hydrothermal route at 383 K for 10 h from an aqueous solution of ammonium molybdate tetrahydrate (AMT) and metal (M = Ni, Cu, Zn) acetates (Ac) with 1 : 1 or 2 : 1 molar ratios of Mo to M. Our results reveal that the two types of zinc molybdates: α-$ZnMoO_4$, and $Zn_3Mo_2O_9$ have been successfully obtained by simply varying the initial concentration of the growth solution.

Among transition metal molybdates available, the structure of $Cu_3Mo_2O_9$ as well as its precursor lindgrenite $Cu_3(OH)_2(MoO_4)_2$ has attracted increasing attention from a wide range of scientific interests.[10] Over the past several years, different structures of lindgrenite such as microspheres and nanobelts were reported by various methods such as hydrothermal synthesis and electrochemically assisted laser ablation in liquid.[11] However, the research on its formation process is still at the beginning and many problems on optimization and control of the process need to be addressed: (i) involvement of multiple steps, (ii) need of stabilizers, (iii) decrease of crystal size, and (iv) improvement of crystal quality. Therefore, the present work is designed to shed light on the following question: what are important factors affecting the crystal growth and surface feature of $Cu_3Mo_2O_9$? Our experiments gave promising results. Highly monodisperse $Cu_3Mo_2O_9$ micropompons were successfully fabricated through sintering the $Cu_3(OH)_2(MoO_4)_2$ microurchins obtained by an ethylenediaminetetraacetic acid (H_4Y)-mediated hydrothermal route. H_4Y was found to have important advantages for the generation of the highly monodisperse $Cu_3(OH)_2(MoO_4)_2$ microurchins. Furthermore, the concentration of H_4Y and sintering temperatures were determined to play crucial roles in control of size and shape of $Cu_3Mo_2O_9$ micropompons.

Recently, there have been extensively studies in the use of molybdenum-based oxide materials at photocatalysis and lithium-ion batteries.[12] For example, $PbMoO_4$ and $CdMoO_4$ showed good activities for the photodegradation of rhodamine B,[13] and $CoMoO_4$ and $Mn_2Mo_3O_8$ exhibited high reversible capacity and excellent cycling stability in lithium-ion batteries.[14] On the other hand, spherical structure materials have received wide attention in photocatalytic degradation of dyes, photocurrent response and lithium-ion batteries during the past decades.[15] This promotes us to investigate whether the as-obtained highly monodisperse $Cu_3Mo_2O_9$ particles have high application potential in various fields including photocatalysis, photocurrent and energy conversion. On testing them, satisfactory results were achieved. First, the $Cu_3Mo_2O_9$ micropompon material showed an excellent photocatalytic activity for Congo red (CR) (>99%) and a very low activity for rhodamine 6G (R6G) (<5%), thereby suggesting excellent photocatalytic efficiency and high catalytic selectivity for organic pollutants. Second, the transient photocurrent response experiment of the material revealed high light current-dark current ratio and stable photocurrent density response, which could be used in future photoelectric response devices. To the best of our knowledge, this is the first application of this family of molybdates in photocurrent response. Third, although the $Cu_3Mo_2O_9$ material had a relatively low reversible capacity than some transition metal oxide materials, but excellent charge–discharge stability and very high coulombic efficiency pointed to a great potential for the use of electrode materials.

In short, this study provides the first report of successful growth of highly monodisperse $Cu_3Mo_2O_9$ micropompons through an H_4Y-assisted synthesis, and gives insights into the applications of the material in three different aspects. It can be predicted that this material will have promising applications in semiconductor photoelectric conversion device and lithium-ion batteries in the future.

2. Experimental

2.1 Materials

AMT, $Cu(Ac)_2 \cdot H_2O$, $Ni(Ac)_2 \cdot 4H_2O$, $Zn(Ac)_2 \cdot 2H_2O$, H_4Y and ethylenediaminetetraacetic acid disodium salt (Na_2H_2Y) were obtained from Shanghai Chemical Reagent. Congo red (CR) and rhodamine 6G (R6G) were obtained from Aladdin Chemistry Co. Ltd. lead. All the chemicals were of general-purpose reagent grade unless otherwise stated.

2.2 Preparation of the transition metal molybdates

First, 0.44 g (0.36 mmol) AMT and 0.50 g (2.50 mmol) $Cu(Ac)_2 \cdot H_2O$ were dissolved together in 40 mL deionized water and stirred at room temperature for 30 min to form a suspension solution. Then the solution was transferred into a Teflon-lined stainless steel autoclave and maintained at 383 K for 10 h. Finally, the green product lindgrenite $Cu_3(OH)_2(MoO_4)_2$ was collected, washed with deionized water and ethanol for several times, and dried at vacuum at 333 K for 12 h. The other series precursors: $NiMoO_4 \cdot xH_2O$, $ZnMoO_4 \cdot 0.8H_2O$ and $Zn_3(OH)_2(MoO_4)_2$ were prepared as the same method but with different materials $Ni(Ac)_2 \cdot 4H_2O$ or $Zn(Ac)_2 \cdot 2H_2O$. The series transition metal molybdates α-$NiMoO_4$, α-$ZnMoO_4$ and $Cu_3Mo_2O_9$, $Zn_3Mo_2O_9$ were obtained by sintering their corresponding precursors at 873 K for 3 h in air.

The $Cu_3(OH)_2(MoO_4)_2$ microurchins were obtained by introducing H_4Y to the mixed solution of AMT with $Cu(Ac)_2 \cdot H_2O$ through a similar synthesis route as mentioned above. Subsequently, sintering the precursor $Cu_3(OH)_2(MoO_4)_2$ at 873 K for 3 h in air leads to the formation of highly monodisperse $Cu_3Mo_2O_9$ micropompon material.

2.3 Photocatalytic measurement

The photocatalytic activities of the monodisperse $Cu_3Mo_2O_9$ micropompon material for the degradation of CR were evaluated by under visible light irradiation. In a typical experiment, 5 mg $Cu_3Mo_2O_9$ was added to a CR solution (10 mL, 50 mg L^{-1} in distilled water) and magnetically stirred in the dark for 30 min to ensure adsorption equilibrium between the solutions and the photocatalysts. Finally, the catalyst was separated by centrifugation (12 000 rpm) and the supernatant solutions were analysed with UV-Vis spectroscopy.

2.4 Photoresponse measurement

The $Cu_3Mo_2O_9$ micropompons were coated on the indium–tin oxide (ITO) electrode. The electrode was immersed in saturated Na_2SO_4 solution. Current-time curves were acquired by a electrochemical analyzer system, CHI760 (Chenhua, Shanghai, China) in a three-compartment cell with a working electrode, a platinum plate counter electrode and a saturated calomel electrode reference electrode under a bias voltage of 0.5 V using the excitation light of Xe lamp (PLS-SXE300, 300 W) as the light source.

2.5 Electrochemical test

Electrode for electrochemical studies was prepared by mixing 70 wt% the as-obtained $Cu_3Mo_2O_9$ micropompons, 20 wt% conducting acetylene black, and 10 wt% polyvinylidene fluoride in N-methylpyrrolidone. The slurry was pasted on a clean copper foil, and dried *in vacuo* at 373 K for 12 h. Subsequently, the coated foil was roll-pressed and cut into a round slice. Test cells were assembled in an argon-filled glove box using lithium foil as the counter electrode and the reference electrode, Celgard 2400 as the separator, and a mixed solution of $LiPF_6$ (1 mol dm^{-3}) with ethylene carbonate, ethyl methyl carbonate and dimethyl carbonate (1 : 1 : 1, v/v/v) as electrolyte. The cells were charged and discharged from 0.01 to 3.00 V at the current density of 100 mA g^{-1} with a LAND CT2001A cell test instrument.

2.6 Instruments and measurements

X-ray diffraction (XRD) measurements were recorded on a Philips X'Pert Pro X-ray diffractometer using a monochromatized Cu Kα radiation source (40 kV, 40 mA) with a wavelength of 0.1542 nm and analyzed in the range $10° \leq 2\theta \leq 70°$. Field emission scanning electron microscope (FE-SEM) images were obtained on a Supra 40 operated at 5 kV.

X-ray photoelectron spectroscopy (XPS) analysis was carried out in a ESCALAB 250 electron spectrometer with a VG Scienta R3000 electron energy analyzer, using Al Kα radiation (1486.6 eV) in ultra-high vacuum (2.00×10^{-9} torr) at room temperature. The energy resolution of the instrument is 0.16 eV. The C1s peak (284.8 eV) was used as the internal standard for binding-energy calibration.

Thermogravimetric (TG) analysis was conducted using a Shimadzu TGA-50 (Shimadzu, Tokyo, Japan) analyser with temperature programmed at a constant heating rate of 10.0 K min^{-1} under an air atmosphere with a gas flow of 25 mL min^{-1}. Fourier transformation infrared (FTIR) spectroscopy was obtained on a Bruker Equinox 55 spectrometer with KBr pellets in the range of 400–4000 cm^{-1} with a resolution of 0.5 cm^{-1}.

Magnetic measurements of samples were carried out on a Quantum Design (QD, San Diego, USA) Magnetic Property Measurement System (MPMS-7XL) equipped with a superconducting quantum interference device (SQUID) by means of a vibrating sample magnetometer.

UV-Vis spectra were measured on a Shimadzu UV 2401 spectrometer in the range 200–700 nm. Photoluminescence (PL) measurement was performed on a Perkin Elmer Luminescence spectrometer L550B at room temperature.

3. Results and discussion

3.1 Structure and morphology of several transition metal molybdates

Fig. 1 shows the XRD patterns of the molybdates α-$NiMoO_4$, $Cu_3Mo_2O_9$ and $Zn_3Mo_2O_9$, as well as their precursors (Fig. S1, ESI†), are crystalline, and consist of a single phase. Therefore, these transition metal molybdates seem to have a general formula: $B_3Mo_2O_9$ (B = Cu and Zn). As for the Ni-system, the
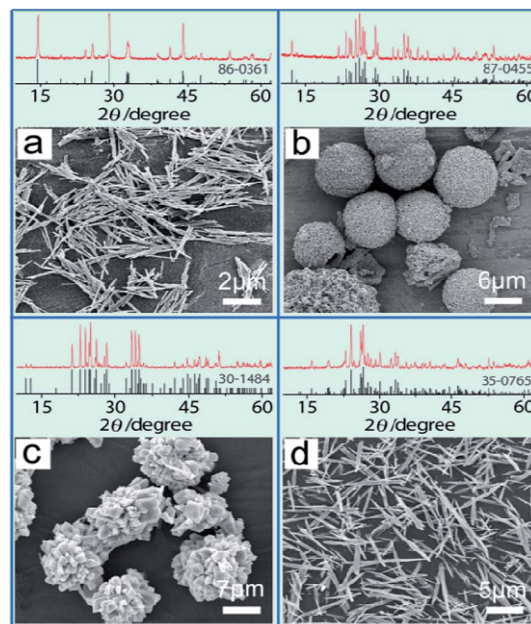

Fig. 1 XRD patterns and FE-SEM images of the α-$NiMoO_4$ (a), $Cu_3Mo_2O_9$ (b), $Zn_3Mo_2O_9$ (c) and α-$ZnMoO_4$ (d).

expected $Ni_3Mo_2O_9$ formulation was not generated. This gives an impression that the composition of the series of molybdates as well as their precursors is closely associated with the structure of the transition metals.

FE-SEM images show that the α-$NiMoO_4$ (Fig. 1a) and its precursor (Fig. S2, ESI†) exhibit a rod-like structure with a diameter of less than 200 nm, while the $B_3Mo_2O_9$ materials, as well as their precursors (Fig. S3, ESI†), present a sphere-like structure (B = Cu, nonuniform microspheres, Fig. 1b; Zn, spherical agglomerates formed by irregular particles, Fig. 1c). This behaviour, that is, 1D structure for $AMoO_4$ and 3D structure for $B_3Mo_2O_9$,[16,17] is closely related to their crystallographic structures of these transition metal molybdates. According to the chemical bonding theory of single crystal growth,[18–20] crystallographic structure thermodynamically determines the growth habit of condensed matters. Therefore, we can follow the intrinsic crystallographic restriction and kinetically tune the growth rate of specific crystal planes *via* varying the growth parameters.

It should be noted that each of the as-obtained molybdates has a similar morphology and size as its respective precursor, suggesting a high structural stability. In particular, the as-obtained $Cu_3Mo_2O_9$ microspheres display a much lower diameter (about 12 μm) than that obtained from $NaMoO_4$,[11] indicating that reaction parameters played a significant role in mediating the formation of molybdate structures. In order to better understand this point, we began a series of experiments aimed at providing a possible route to obtain highly monodisperse particles with good size and shape uniformity.

Initially, we performed a group of new preparation experiments at the same conditions but using a 2 : 1 molar ratio of Mo to M (Ni, Cu and Zn). A very interesting result is that pure anorthic α-$ZnMoO_4$ (Fig. 1d) and its precursor $ZnMoO_4 \cdot 0.8H_2O$

(Fig. S4, ESI†) were obtained while Ni and Cu still produced the same results as obtained with a 1 : 1 molar ratio (Fig. S5, ESI†). The as-obtained α-ZnMoO$_4$, like its precursor (Fig. S6, ESI†), has a 1D rod-like structure with a width of about 400 nm and a mean length of 15 μm. This is one of a few examples available of initial concentration-dependent structural response of transition metal molybdates.[21] The origin of this response is still not clear at present but it may be in connection with the different ratios of Mo to M in the two kinds of molybdates. A high initial molar ratio of Mo to M (2 : 1) leads to the creation of 1D ZnMoO$_4$·0.8H$_2$O (atom number ratio of Mo and M, 1 : 1). On the contrary, a low molar ratio (1 : 1) causes the formation of Zn$_3$Mo$_2$O$_9$ (atom number ratio of Mo and M, 2 : 3). This phenomenon does not occur in the cases of Ni and Cu, strongly implying unusual condition dependence of the formation process of molybdates.

3.2 Formation process of highly monodisperse Cu$_3$Mo$_2$O$_9$ micropompons

Subsequently, to elucidate the formation process, we select the microspherical Cu$_3$Mo$_2$O$_9$ as a representative of the molybdates to study its generation and morphology evolution. Growth experiments (Fig. S7, ESI†) of its precursor Cu$_3$(OH)$_2$(MoO$_4$)$_2$ were performed at 383 K for heating times of 0.5, 1, 3, 5 and 10 h with a 1 : 1 initial molar ratio of Mo to Cu. There is a clear evolution from a pure anorthic (NH$_4$)$_2$Cu(MoO$_4$)$_2$ at 0.5 h (eqn (1)) to a mixture of (NH$_4$)$_2$Cu(MoO$_4$)$_2$ and the precursor at 1 and 3 h, and finally to the pure precursor at 10 h (eqn (2), Route I in Fig. 2). The precursor was then sintered to form the final structure (eqn (3), Route I). The (NH$_4$)$_2$Cu(MoO$_4$)$_2$ with a nanoplate-like structure (diameter, 100 nm) can be regarded as an intermediate of the microspherical precursor,[7b] since we observed that almost only Cu$_3$(OH)$_2$(MoO$_4$)$_2$ was present at the heating time of 5 h. This fact that such a shape change with increasing heating times is accompanied by a structural transformation may reflects a gradual self-assembly process.

$$Cu^{2+} + 2NH_4^+ + 2MoO_4^{2-} \rightarrow (NH_4)_2Cu(MoO_4)_2 \quad (1)$$

$$(NH_4)Cu(MoO_4)_2 + 2Cu^{2+} + 2H_2O \rightarrow Cu_3(OH)_2(MoO_4)_2 \\ + 2NH_4^+ + 2H^+ \quad (2)$$

$$Cu_3(OH)_2(MoO_4)_2 \rightarrow Cu_3Mo_2O_9 + H_2O \quad (3)$$

$$3Cu^{2+} + 2MoO_4^{2-} + 2H_2O \rightarrow Cu_3(OH)_2(MoO_4)_2 + 2H^+ \quad (4)$$

$$Cu^{2+} + H_4Y \rightleftharpoons CuY^{2-} + 4H^+ \quad (5)$$
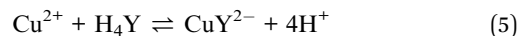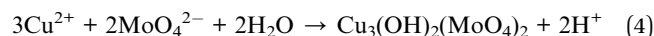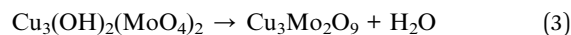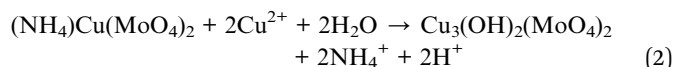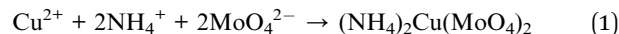
When water was replaced by anhydrous ethanol in the synthesis, only pure (NH$_4$)$_2$Cu(MoO$_4$)$_2$ (Fig. S8, ESI†) with a sphere-like morphology (diameter, 3 μm; Fig. S9, ESI†) was obtained even at the heating time of 10 h. This confirms that the microspherical structure of the precursor was originated from the self-assembly of the nanoplates in aqueous solution. These findings demonstrate that at early stage of the solvothermal process, Cu^{2+} was first reacted with NH$_4^+$ and MoO$_4^{2-}$ arising from the dissociation of AMT in water (pH, about 4.5),[22] leading to the formation and rapid growth of the intermediate (eqn (1)). The intermediate was then hydrolyzed to produce the precursor in the presence of Cu^{2+} (eqn (2)). The formation of the intermediate could be an important reason for the relatively small size of the microspheres when compared to those reported by Xu and Xue.[11a]

Although the as-obtained Cu$_3$Mo$_2$O$_9$ exhibits a microspherical structure, we have so far not succeeded in obtaining highly monodisperse fractions. A possible reason is that the self-assembly process of the intermediate nanoplates in the early time is not pronounced. Thus, we tried to decrease pH in solution in order to restrain the formation of the intermediate. Our result indicate that in a moderate acidity [pH, 2–4, HCl, HAc and H$_4$Y], (NH$_4$)$_2$Cu(MoO$_4$)$_2$ crystals did not form, but Cu$_3$(OH)$_2$(MoO$_4$)$_2$ crystals (Fig. S10, ESI†) still can be obtained
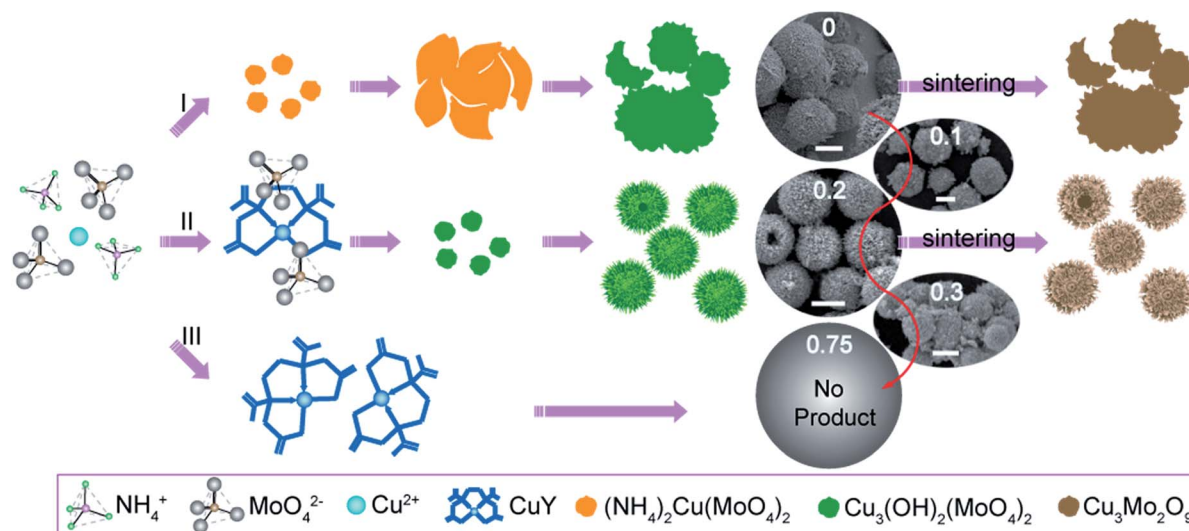

Fig. 2 Schematic illustration describing the formation of the Cu$_3$Mo$_2$O$_9$ materials. The FE-SEM images were obtained by adding H$_4$Y of 0, 0.1, 0.2, 0.3 and 0.75 g. The white scale bars were 8 μm.

(eqn (4), Route II in Fig. 2). This finding strongly suggests that acidity is a major component to directly producing a stable precursor. As seen from eqn (4), the generation of the precursor further causes a decrease of pH. A comparison of the effect of these acids on the crystallization of the precursor reveals that the addition of H_4Y gives a very positive and encouraging result, while at the same conditions, HCl and HAc led to large size and poor quality of materials (Fig. S11, ESI†).

Fig. 3a presents the FE-SEM image of the $Cu_3(OH)_2(MoO_4)_2$ obtained by introducing H_4Y (0.2 g) into the solution of AMT and $Cu(Ac)_2$ as a chelating agent. XRD analysis (Fig. S12, ESI†) indicates that it is a pure phase without any heterogeneity. As seen from this figure, highly monodisperse microspherical particles were successfully constructed. The magnified images in Fig. 3b and c look like an urchin structure (Fig. 3d). It is interesting to notice that both higher and lower concentrations of H_4Y resulted in the formation of larger size particles (diameter > 10 μm, Fig. S13 and S14, ESI†). In particular, adjacent particles have a marked tendency to gather together at a higher concentration of H_4Y (0.3 g). More importantly, when the amount of H_4Y was increased to 0.75 g, there is no precipitation of $Cu_3(OH)_2(MoO_4)_2$ (Route III in Fig. 2).

These observations give an indication that the introduction of H_4Y, a strong competitive chelating ligand, played a pivotal role in prohibiting the formation of $(NH_4)_2Cu(MoO_4)_2$, creating such a monodisperse structure of $Cu_3(OH)_2(MoO_4)_2$ and

decreasing the size of the structure (Route II). We consider that they are associated with the formation of the complex CuY.

It is well-known that CuY is sufficiently stable and its formation will result in the release of protons, decreasing the pH of solution. High stability means the possibility to reduce the free concentration of Cu^{2+} ions in the aqueous phase. As a result, two kinds of equilibria will be established in the solution, precipitation equilibrium (eqn (4)) and coordination equilibrium (eqn (5)). This allows a gradual dissociation of the complex to produce Cu^{2+} ions, thereby causing slow, more uniform growth of $Cu_3(OH)_2(MoO_4)_2$ (Route II). Control experiments demonstrated this. While Na_2H_2Y was introduced into the system (pH, 5), the as-obtained $(NH_4)_2Cu(MoO_4)_2$ exhibits smaller size and better quality when compared to that obtained by Route I in Fig. 2 (Fig. S15, ESI†).

Thermogravimetric (TG) analysis in air (Fig. S16, ESI†) indicates that the dehydration reaction (eqn (3)) of the microurchin precursor occurs at below 678 K. Fig. 3e shows the FE-SEM image of the orthorhombic $Cu_3Mo_2O_9$ (Fig. S12, ESI†) obtained by sintering the microurchins at 873 K for 3 h. Like its precursor, it also exhibits microstructure (Fig. 3f) with a diameter of about 8 μm and has a highly monodisperse particle size distribution. The magnified image in Fig. 3g of a single microsphere look like a pompon (Fig. 3h). The FTIR bands (Fig. S17, ESI†) of the $Cu_3Mo_2O_9$ micropompon material at 531, 718, 776, 818, 902, 942, 969, 1635 and 3440 cm^{-1} are in good agreement with previous results reported by Xu and Xue.[11a] No peak of impurity was found in the spectrum, confirming that the material is pure.

Fig. 4a shows the XPS survey spectrum of the $Cu_3Mo_2O_9$ micropompons, in which Cu, Mo and O are observable, and no impurities were detected. Fig. 4b presents the peaks of Cu $2p_{3/2}$ at the binding energies of 934.0 eV and Cu $2p_{1/2}$ at 954.1 eV, which are the same as those reported in the literature.[23] In the narrow scan spectrum of Mo 3d (Fig. 4c), there are two peaks with binding energies at 232.4 and 235.5 eV due to Mo $3d_{5/2}$ and
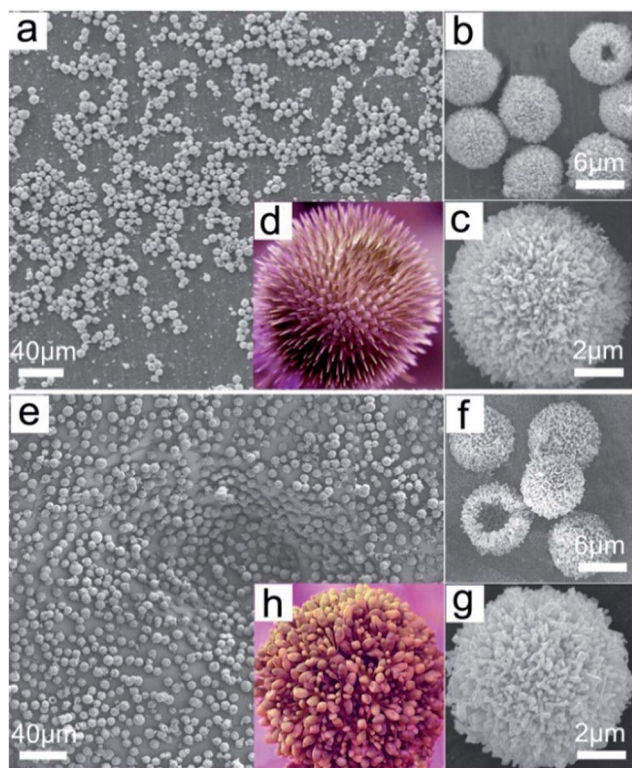
Fig. 3 FE-SEM images of highly monodisperse $Cu_3(OH)_2(MoO_4)_2$ (a) and $Cu_3Mo_2O_9$ (e); higher-magnification of a group of microurchins (b), a single microurchin (c), a group of micropompons (f), a signal micropompon (g); and photos of an urchin (d) and a pompon (h).
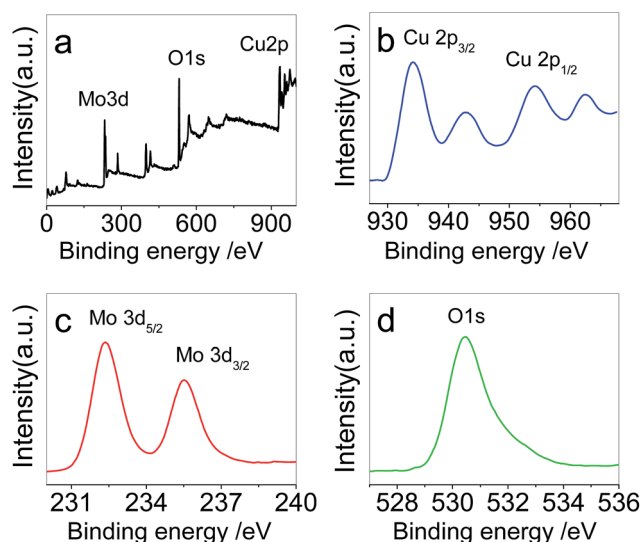

Fig. 4 XPS survey spectrum of the $Cu_3Mo_2O_9$ micropompons (a), XPS spectra of Cu 2p (b), Mo 3d (c) and O 1s peaks (d) of the material.

Mo $3d_{3/2}$ in Mo(VI), respectively.[24] The peak areas and use of atomic sensitivity factors provide that the Cu/Mo molar ratio is about 3 : 2. Moreover, a strong O peak is positioned at about 530.4 eV (Fig. 4d). These data confirm that the composition of the material is in good accordance with the result of XRD.

Also, we performed sintering experiments at different temperatures: 773 and 973 K for 3 h to investigate the dehydration characteristics of the microurchin precursor. Our result indicates the sintering products at the temperatures are pure $Cu_3Mo_2O_9$ and have the same orthorhombic crystal structure as the microurchins (Fig. S18, ESI†). FE-SEM images (Fig. S19, ESI†) show that the materials adopt a similar spherical geometry (diameter, 8 μm) as that obtained at 873 K, but there is a clear shape transition process in surface features from a large number of very fine wires at 773 K to small rods at 873 K and finally to thin patches all over the surface at 973 K, as a consequence of Ostwald ripening and coalescence.[25]

3.3 Optical and magnetic properties of the monodisperse $Cu_3Mo_2O_9$ micropompons

Fig. 5 indicates the PL spectrum of the $Cu_3Mo_2O_9$ micropompon material at the excitation wavelength of 325 nm. Clearly, the $Cu_3Mo_2O_9$ has a very strong emission band at 436 nm (2.84 eV) and a prominent shoulder at 417 (2.97 eV). The former is due to the band-to-band transition in Mo–O units and the latter is due to Cu(II) in the material.[26]

The relationship between the magnetization (M) *versus* magnetic field (H) and temperature (T) of the $Cu_3Mo_2O_9$ micropompons were measured by SQUID. Fig. 6a shows the M–H curve of the material at 2 K in the range from −50 to 50 KOe, without a saturated magnetization. A narrow hysteresis loop occurs between −8 and +8 KOe was observed, with a linear increase above 8 KOe, indicating a typical ferromagnetism characteristic. Below 40 K, there is a broad signal centered at 20.5 K. Vilminot and collaborators suggested that it could be associated with 1D or 2D short-range antiferromagnetic correlation.[10c]

However, above 40 K, this material presents typical characteristics of superparamagnetism, which is different from that of bulk CuO as it exhibits an antiferromagnetic property.[27] A probable reason is the relatively complex structure of Cu–O bonds in the material. Further, SQUID (Fig. S20, ESI†) analysis of the $Cu_3(OH)_2(MoO_4)_2$ microurchin material indicates that it is
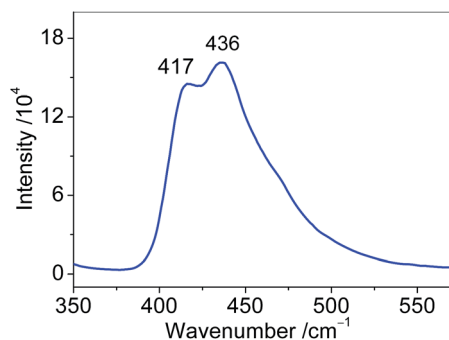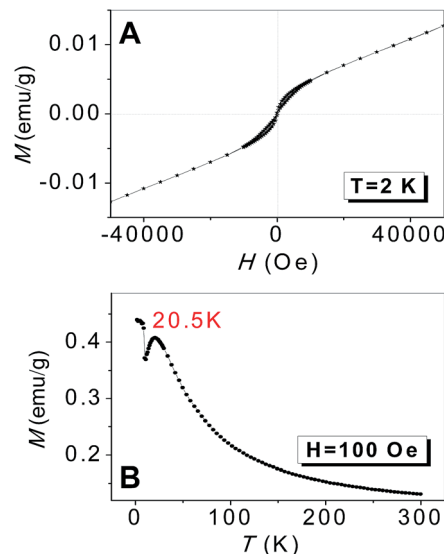
Fig. 6 Magnetic hysteresis loops of the $Cu_3Mo_2O_9$ micropompons at 2 K in the applied fields: from −50 000 to 50 000 Oe (A) and temperature dependence of magnetization of the $Cu_3Mo_2O_9$ micropompons at 100 Oe in field-cooling (FC) processes from 2 to 300 K (B).

ferromagnetic at 2 K, with coercive field and remanent magnetization and Curie temperature of about 6.0 KOe, 5.7×10^{-2} emu g^{-1} and 13.4 K, respectively, which is in agreement with recent reports.[11b,28] The results strongly suggest that the $Cu_3Mo_2O_9$ has different magnetization manners from its precursor, which might be related with their individual crystal structures.

To further understand the relationship between structure and properties of the $Cu_3Mo_2O_9$ micropompon material, we performed Brunauer–Emmett–Teller[29] (BET) specific surface area measurements. Its BET surface area was calculated to be 4.2 m^2 g^{-1} (Fig. S21, ESI†). In addition, its Barrett–Joyner–Halenda[30] (BJH) pore size was determined to be 17 nm, based on the isotherms of the adsorption–desorption of N_2. Large surface area and small pore size enable us to investigate its application in photocatalytic removal of organic pollutants, lithium storage performance and photoresponse properties.

3.4 Photocatalytic properties of the monodisperse $Cu_3Mo_2O_9$ micropompons

Here, CR,[31] a carcinogenic direct diazo dye used for the coloration of paper products, was chosen as the model organic pollutant. Fig. 7A shows the UV-Vis adsorption spectra of the solutions of CR (initial concentration fixed at 50 mg L^{-1}) after being treated with 5 mg $Cu_3Mo_2O_9$ micropompons at different light irradiation times (from 0 to 150 min, fiercely stirred for 30 min in the room temperature to ensure the adsorption–desorption equilibrium). As shown in the figure, CR has a strong band at 496 nm and a moderate band at 345 nm, corresponding to $n \rightarrow \pi^*$ transition of the N atoms in the azo group and $\pi \rightarrow \pi^*$ transition of the aromatic rings, respectively.[32]

Fig. 5 PL spectrum of the $Cu_3Mo_2O_9$ micropompons.
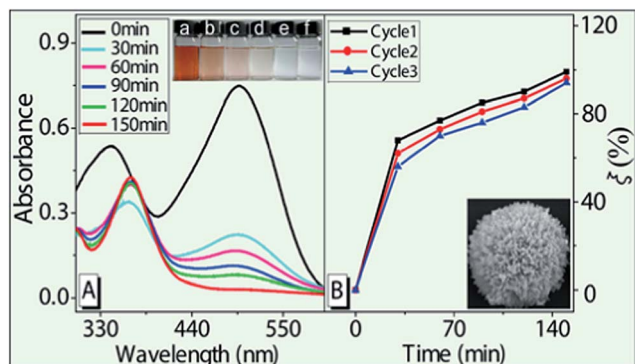
Fig. 7 UV-Vis absorption spectra of the CR (A) solutions after being treated by the $Cu_3Mo_2O_9$ micropompons using different time intervals; the photodegradation degree of CR in the first three cycles (B). The inset in (A) shows a colour change of the CR solutions from 30 (a) to 150 (f) min in the first cycle. The inset in (B) was the crystal morphology of a $Cu_3Mo_2O_9$ micropompon after the first three cycles for the photodegradation of CR.

The band at 496 nm was used to examine the effect of photocatalytic degradation. Clearly, the absorbance of the CR solutions got smaller and smaller with increasing irradiation time. After an irradiation of 150 min, the strong absorption peak almost completely disappeared. The shift of the peak at 345 nm may be due to the structure change of the CR molecule during the photocatalytic process, accompanying with the cleavage of the azo bond and the generation of amino groups. The structural transformation of auxochromes from azo group to amino group on the chromophore (aromatic ring) is responsible for the band shift in the UV–Vis absorption spectra.[33] The gradual colour change of the series solutions was clearly expressed by a photograph (the inset of Fig. 7A). The photodegradation degree (ξ, %) of CR were calculated based on eqn (6).

$$\xi = [(C_0 - C)/C_0] \times 100\% \tag{6}$$

In this equation, C_0 is the initial concentration of CR, and C is the real concentration of CR after light irradiation for a certain period. The ξ value of CR after an irradiation of 150 min in the presence of the $Cu_3Mo_2O_9$ micropompons is 99.1%, and especially that the ξ values over the first three cycles still can be maintained above 95.0%, as shown in Fig. 7B.

The hierarchical morphology of the catalyzer can be still maintained as shown in the inset of Fig. 7B after three consecutive cycles, revealing its high structure stability and good catalytic sustainability. It is worth stressing that when CR was substituted by R6G, the $Cu_3Mo_2O_9$ micropompons showed very low degradation ability (ξ, 3.7%) even at a light irradiation time of 150 min (Fig. S22, ESI†). This may be explained by the fact that CR is an anionic dye with a high affinity for the catalyzer particles with negative charges while the R6G is cationic dyes.[34] These results strongly demonstrate that the $Cu_3Mo_2O_9$ material has excellent photocatalytic efficiency, good stability and high catalytic selectivity for organic pollutants.

3.5 Photocurrent response of the monodisperse $Cu_3Mo_2O_9$ micropompons

To confirm that there is a transfer of photogenerated electrons and especially that there is a high concentration of electron–hole pairs and electron–hole pair emigration to surface of the $Cu_3Mo_2O_9$ micropompon material, the transient photocurrent response experiment was carried out on a photo electro-chemical test device fabricated by spin coating the alcohol solution of the $Cu_3Mo_2O_9$ onto an ITO electrode illuminated with a light on/off circle of 120 s and a bias potential of 0.5 V.

Fig. 8 shows the time-dependent photoresponse of the $Cu_3Mo_2O_9$ micropompon material. Several interesting and unexpected phenomena were observed from the current density–time profile. First, a low dark current (0.11 μA cm^{-2}) indicates the very low density of dislocations and point defects in the material. Second, upon illumination, it immediately jumps to a constant much higher value of 18.8 μA cm^{-2} (light current), thereby giving a very high ratio (about 171) of light current to dark current. Third, the photocurrent density response of this material is reversible and stable, indicating that the photocurrent may be reproduced for each irradiation. In short, such a large light current under a bias voltage of 0.5 emphasizes the lower recombination of electron–hole pairs and efficient photoelectron emigration.[35] High light current-dark current ratio could be used in future photoelectric response devices. This may be a reason for the strong photocatalytic activity of this material. To the best of our knowledge, this is the first application of this family of molybdates in photocurrent response.

3.6 Lithium storage performances of the monodisperse $Cu_3Mo_2O_9$ micropompons

Fig. 9A shows the charge–discharge curves of the $Cu_3Mo_2O_9$ micropompons in the voltage range from 0.01 to 3.00 V at a constant current density of 100 mA g^{-1}. It delivers discharge capacities of 1224, 437, and 272 mA h g^{-1} and charge capacities 432, 279, and 221 mA h g^{-1} during the first, second, and third cycles, respectively.
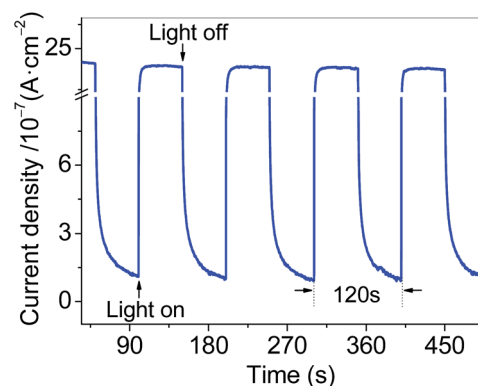

Fig. 8 Current response vs. time for the $Cu_3Mo_2O_9$ micropompons under chopped irradiation at a bias potential of 0.5 V.

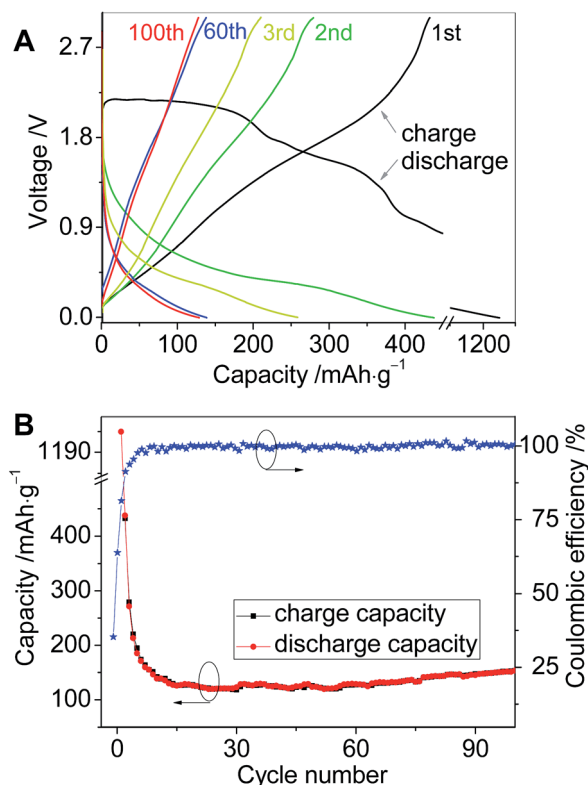Fig. 9 Charge–discharge voltage profiles of the $Cu_3Mo_2O_9$ micropompons at a current density of 100 mA g^{-1} (A). Cycling performance and coulombic efficiency of the $Cu_3Mo_2O_9$ micropompons at a current density of 100 mA g^{-1} (B).

We noticed that there is a drastic decrease of the initial capacities from a first cycle to a subsequent cycle in the three cycles. A possible reason may be the relatively large grain size of the material. The other reason could be that Cu(II) and Mo(VI) ions contribute to the irreversible capacity loss, probably through a mechanism similar to the formation of a solid electrolyte interface (SEI) on the surface of the electrode.[36]

It was reported that the lithium storage mechanism of transition metal molybdates was associated with the formation of Li–A–O (A = Ni, Co and Cu) and Li_xMoO_y in the first discharge. We consider that lithium ions can enter the $Cu_3Mo_2O_9$ crystallites through an irreversible copper reduction and the formation of Li_xMoO_y phase.[37] The generation of the irreversible Li–Cu–O is partly responsible for the initial irreversible capacity loss in the first cycle.[38] In the following charge–discharge cycles, the electrochemically active Li_xMoO_y delivers reversible electrochemical reactivity towards Li.[39] Especially, the charge–discharge values of the battery were kept stable after the 11th cycle, indicating a high coulombic efficiency during the reversible formation/decomposition of the Li_xMoO_y phase.

Fig. 9B shows the cycle performance and coulombic efficiency of the $Cu_3Mo_2O_9$ at a current density of 100 mA g^{-1}. The specific capacity first decreases quickly (from cycle 1 to cycle 10) and then reaches a plateau (from cycle 11 to cycle 100). It is worthy of noting that after 60 cycles, the reversible capacity of the material is still up to 129 mA h g^{-1}, which is comparable to

values obtained for $NiMoO_4$ by others.[39] In particular, this battery exhibits extremely high coulombic efficiency (higher than 99%), even after 100 charge–discharge cycles. Further, there is a dropping-rising phenomenon of the capacity in the cycling performance of the material (100th cycle, 153 mA h g^{-1}), which may be due to the electrochemical activation of the electrode material during the cycles.[40] This is the first example of the $B_3Mo_2O_9$ type materials for lithium storage capability. Although it has a relatively low reversible capacity but excellent charge–discharge stability and very high coulombic efficiency suggest a great potential for the use of electrode materials.

4. Conclusions

In summary, the present work not only provides the first evidence that the generation of α-$ZnMoO_4$ and $Zn_3Mo_2O_9$ is dependent on the initial concentration of reactants, but also successfully fabricates highly monodisperse $Cu_3Mo_2O_9$ micropompons through an H_4Y-mediated hydrothermal method and subsequent sintering. The as-obtained $Cu_3Mo_2O_9$ micropompons present an excellent photocatalytic efficiency and selectivity for organic dyes. Large photocurrent density and especially high light current-dark current ratio suggest that it has a potential used as a semiconductor photoelectric conversion device. Outstanding charge–discharge stability and extremely high coulombic efficiency is an indicative of a potential ability to act as electrode materials in lithium-ion batteries.

Acknowledgements

Notes and references

1 (a) D. Guo, P. Zhang, H. M. Zhang, X. Z. Yu, J. Zhu, Q. H. Li and T. H. Wang, *J. Mater. Chem. A*, 2013, **1**, 9024; (b) M. C. Liu, L. B. Kong, C. Lu, X. J. Ma, X. M. Li, Y. C. Luo and L. Kang, *J. Mater. Chem. A*, 2013, **1**, 1380; (c) J. Baek, A. S. Sefat, D. Mandrus and P. S. Halasyamani, *Chem. Mater.*, 2008, **20**, 3785.

2 (a) X. Z. Yu, B. A. Lu and Z. Xu, *Adv. Mater.*, 2014, **26**, 1044; (b) C. T. Cherian, M. V. Reddy, S. C. Haur and B. V. R. Chowdari, *ACS Appl. Mater. Interfaces*, 2013, **5**, 918; (c) L. Zhang, X. F. Cao, Y. L. Ma, X. T. Chen and Z. L. Xue, *CrystEngComm*, 2010, **12**, 207; (d) L. Q. Mai, F. Yang, Y. L. Zhao, X. Xu, L. Xu and Y. Z. Luo, *Nat. Commun.*, 2011, **2**, 381.

3 (a) J. X. Cui, W. S. Wang, L. Zhen, W. Z. Shao and Z. L. Chen, *CrystEngComm*, 2012, **14**, 7025; (b) A. E. Thiry, M. Gaudon, C. Payen, N. Daro, J. F. Letard, S. Gorsse, P. Deniard, X. Rocquefelte, A. Demourgues, M. H. Whangbo and S. Jobic, *Chem. Mater.*, 2008, **20**, 2075.

4 (a) W. G. Chu, H. F. Wang, Y. J. Guo, L. N. Zhang, Z. H. Han, Q. Q. Li and S. S. Fan, *Inorg. Chem.*, 2009, **48**, 1243; (b) M. Matsumoto, H. Kuroe, T. Sekine and M. Hase, *J. Phys.*

Soc. Jpn., 2012, **81**, 024711; (*c*) W. Reichelt, U. Steiner, T. Sohnel, O. Oeckler, V. Duppel and L. Kienle, *Z. Anorg. Allg. Chem.*, 2005, **631**, 596.

5 (*a*) C. Mazzocchia, C. Aboumrad, C. Diagne, E. Tempesti, J. M. Herrmann and G. Thomas, *Catal. Lett.*, 1991, **10**, 181; (*b*) H. M. AbdelDayem and M. A. Al-Omair, *Ind. Eng. Chem. Res.*, 2008, **47**, 1011; (*c*) Y. Chen, F. Meng, C. Ma, Z. W. Yang, C. L. Zhu, Q. Ouyang, P. Gao, J. Q. Li and C. W. Sun, *J. Mater. Chem.*, 2012, **22**, 12900.

6 (*a*) L. S. Cavalcante, E. Moraes, M. A. P. Almeida, C. J. Dalmaschio, N. C. Batista, J. A. Varela, E. Longo, M. S. Li, J. Andres and A. Beltran, *Polyhedron*, 2013, **54**, 13; (*b*) Y. Liang, P. Liu, H. B. Li and G. W. Yang, *Cryst. Growth Des.*, 2012, **12**, 4487.

7 (*a*) D. P. Cai, D. D. Wang, B. Liu, Y. R. Wang, Y. Liu, L. L. Wang, H. Li, H. Huang, Q. H. Li and T. H. Wang, *ACS Appl. Mater. Interfaces*, 2013, **5**, 12905; (*b*) J. S. Xu, D. F. Xue and Y. C. Zhu, *J. Phys. Chem. B*, 2006, **110**, 17400; (*c*) D. Ghosh, S. Giri and C. K. Das, *Nanoscale*, 2013, **5**, 10428.

8 (*a*) G. S. R. Raju, E. Pavitra, Y. H. Ko and J. S. Yu, *J. Mater. Chem.*, 2012, **22**, 15562; (*b*) T. Grewe, X. H. Deng, C. Weidenthaler, F. Schuth and H. Tuysuz, *Chem. Mater.*, 2013, **25**, 4926; (*c*) G. Ahmad, M. B. Dickerson, B. C. Church, Y. Cai, S. E. Jones, R. R. Naik, J. S. King, C. J. Summers, N. Kroger and K. H. Sandhage, *Adv. Mater.*, 2006, **18**, 1759; (*d*) Y. S. Luo, W. D. Zhang, X. J. Dai, Y. Yang and S. Y. Fu, *J. Phys. Chem. C*, 2009, **113**, 4856.

9 (*a*) C. Peng, L. Gao, S. W. Yang and J. Sun, *Chem. Commun.*, 2008, 5601; (*b*) A. Klisinska, A. S. Mamede and E. M. Gaigneaux, *Stud. Surf. Sci. Catal.*, 2006, **162**, 745.

10 (*a*) J. C. Hill, Y. Ping, G. A. Galli and K. S. Choi, *Energy Environ. Sci.*, 2013, **6**, 2440; (*b*) H. Kuroe, T. Hamasaki, T. Sekine, M. Hase, K. Oka, T. Ito, H. Eisaki, K. Kaneko, N. Metoki, M. Matsuda and K. Kakurai, *Phys. Rev. B: Condens. Matter Mater. Phys.*, 2011, **83**, 184423; (*c*) S. Vilminot, G. Andre and M. Kurmoo, *Inorg. Chem.*, 2009, **48**, 2687.

11 (*a*) J. S. Xu and D. F. Xue, *J. Solid State Chem.*, 2007, **180**, 119; (*b*) P. Liu, Y. Liang, X. Z. Lin, C. X. Wang and G. W. Yang, *ACS Nano*, 2011, **5**, 4748.

12 (*a*) A. F. Gouveia, J. C. Sczancoski, M. M. Ferrer, A. S. Lima, M. R. M. C. Santos, M. S. Li, R. S. Santos, E. Longo and L. S. Cavalcante, *Inorg. Chem.*, 2014, **53**, 5589; (*b*) Z. Xu, Z. Li, X. Tan, C. M. B. Holt, L. Zhang, B. S. Amirkhiz and D. Mitlin, *RSC Adv.*, 2012, **2**, 2753.

13 (*a*) W. S. Wang, L. Zhen, C. Y. Xu, W. Z. Shao and Z. L. Chen, *CrystEngComm*, 2013, **15**, 8014; (*b*) M. R. D. Bomio, R. L. Tranquilin, F. V. Motta, C. A. Paskocimas, R. M. Nascimento, L. Gracia, J. Andres and E. Longo, *J. Phys. Chem. C*, 2013, **117**, 21382.

14 (*a*) C. T. Cherian, M. V. Reddy, S. C. Haur and B. V. R. Chowdari, *ACS Appl. Mater. Interfaces*, 2013, **5**, 918; (*b*) Y. M. Sun, X. L. Hu, W. Luo and Y. H. Huang, *J. Mater. Chem.*, 2011, **21**, 17229.

15 (*a*) D. D. Cai, L. X. Ding, S. Q. Wang, Z. Li, M. Zhu and H. H. Wang, *Electrochim. Acta*, 2014, **139**, 96; (*b*) D. Li, Q. Qin, X. C. Duan, J. Q. Yang, W. Guo and W. J. Zheng,

ACS Appl. Mater. Interfaces, 2013, **5**, 9095; (*c*) R. R. Zhang, Y. Y. He and L. Q. Xu, *J. Mater. Chem. A*, 2014, **2**, 17979.

16 (*a*) Y. Ding, Y. Wan, Y. L. Min, W. Zhang and S. H. Yu, *Inorg. Chem.*, 2008, **47**, 7813; (*b*) S. H. Tian, J. L. Zhang, J. Chen, L. J. Kong, J. Lu, F. C. Ding and Y. Xiong, *Ind. Eng. Chem. Res.*, 2013, **52**, 13333.

17 (*a*) M. C. Liu, L. Kang, L. B. Kong, C. Lu, X. J. Ma, X. M. Li and Y. C. Luo, *RSC Adv.*, 2013, **3**, 6472; (*b*) K. S. Park, S. D. Seo, H. W. Shim and D. W. Kim, *Nanoscale Res. Lett.*, 2012, **7**, 1; (*c*) M. Y. Dong, Q. Lin, H. M. Sun, D. Chen, T. Zhang, Q. Z. Wu and S. P. Li, *Cryst. Growth Des.*, 2011, **11**, 5002.

18 (*a*) C. T. Sun and D. F. Xue, *J. Phys. Chem. C*, 2013, **117**, 5505; (*b*) D. F. Xue, K. Y. Li, J. Liu, C. T. Sun and K. F. Chen, *Mater. Res. Bull.*, 2012, **47**, 2838.

19 C. T. Sun and D. F. Xue, *CrystEngComm*, 2014, **16**, 2129.

20 C. T. Sun and D. F. Xue, *Cryst. Growth Des.*, 2014, **14**, 2282.

21 K. Pavani and A. Ramanan, *Eur. J. Inorg. Chem.*, 2005, 3080.

22 (*a*) K. Y. Li, P. Yang, L. X. Niu and D. F. Xue, *J. Phys. Chem. A*, 2012, **116**, 6911; (*b*) K. Y. Li, M. Li and D. F. Xue, *J. Phys. Chem. A*, 2012, **116**, 4192; (*c*) K. Y. Li and D. F. Xue, *J. Phys. Chem. A*, 2006, **110**, 11332; (*d*) Y. Keereeta, T. Thongtem and S. Thongtem, *Mater. Lett.*, 2012, **68**, 265; (*e*) Y. H. Ding, C. Y. Li and R. Guo, *Ultrason. Sonochem.*, 2010, **17**, 46.

23 (*a*) L. X. Song, J. Yang, L. Bai, F. Y. Du, J. Chen and M. Wang, *Inorg. Chem.*, 2011, **50**, 1682; (*b*) R. T. Figueiredo, A. Martinez, M. L. Granados and J. L. G. Fierro, *J. Catal.*, 1998, **178**, 146.

24 (*a*) B. Li, S. X. Yang, N. J. Huo, Y. T. Li, J. H. Yang, R. X. Li, C. Fan and F. Y. Lu, *RSC Adv.*, 2014, **4**, 26407; (*b*) L. X. Song, J. Xia, Z. Dang, J. Yang, L. B. Wang and J. Chen, *CrystEngComm*, 2012, **14**, 2675.

25 D. Alloyeau, C. Ricolleau, C. Mottet, T. Oikawa, C. Langlois, Y. Le Bouar, N. Braidy and A. Loiseau, *Nat. Mater.*, 2009, **8**, 940.

26 (*a*) J. M. Song, X. M. Ni, D. G. Zhang and H. G. Zheng, *Solid State Sci.*, 2006, **8**, 1164; (*b*) B. V. Kumar and M. Vithal, *Phys. B*, 2012, **407**, 2094; (*c*) X. Q. Liu, Z. Li, C. X. Zhao, W. Zhao, J. B. Yang, Y. Wang and F. Li, *J. Colloid Interface Sci.*, 2014, **419**, 9.

27 (*a*) W. L. Gao, S. H. Yang, S. G. Yang, L. Y. Lv and Y. W. Du, *Phys. Lett. A*, 2010, **375**, 180; (*b*) S. Manna and S. K. De, *J. Magn. Magn. Mater.*, 2010, **322**, 2749.

28 S. Vilminot, G. Andre, M. R. Plouet, F. B. Vigneron and M. Kurmoo, *Inorg. Chem.*, 2006, **45**, 10938.

29 S. Brunauer, P. H. Emmett and E. Teller, *J. Am. Chem. Soc.*, 1938, **60**, 309.

30 E. P. Barrett, L. G. Joyner and P. P. Halenda, *J. Am. Chem. Soc.*, 1951, **73**, 373.

31 (*a*) S. Erdemoglu, S. K. Aksu, F. Sayilkan, B. Izgi, M. Asilturk, H. Sayilkan, F. Frimmel and S. Gucer, *J. Hazard. Mater.*, 2008, **155**, 469; (*b*) M. N. Chong, H. Y. Zhu and B. Jin, *Chem. Eng. J.*, 2010, **156**, 278.

32 (*a*) B. Neumann and P. Pollmann, *Phys. Chem. Chem. Phys.*, 2001, **3**, 4508; (*b*) C. G. Hu, Z. L. Chen, A. G. Shen, X. C. Shen, H. Li and S. S. Hu, *Carbon*, 2006, **44**, 428.

33 (*a*) S. Chopin, F. Chaignon, E. Blart and F. Odobel, *J. Mater. Chem.*, 2007, **17**, 4139; (*b*) S. G. R. Guinot, J. D. Hepworth and

M. Wainwright, *J. Chem. Soc., Perkin Trans.*, 1998, 297; (*c*) T. G. Pavlopoug and P. R. Hammond, *J. Am. Chem. Soc.*, 1974, **96**, 6568.

34 (*a*) H. Lachheb, E. Puzenat, A. Houas, M. Ksibi, E. Elaloui, C. Guillard and J. M. Herrmann, *Appl. Catal., B*, 2002, **39**, 75; (*b*) M. Bootharaju and T. Pradeep, *Langmuir*, 2013, **29**, 8125.

35 (*a*) Q. Zhu, Y. Peng, L. Lin, C. M. Fan, G. Q. Gao, R. X. Wang and A. W. Xu, *J. Mater. Chem. A*, 2014, **2**, 4429; (*b*) C. M. Fan, Y. Peng, Q. Zhu, L. Lin, R. X. Wang and A. W. Xu, *J. Phys. Chem. C*, 2013, **117**, 24157.

36 (*a*) L. Zhang, H. B. Wu, R. Xu and X. W. Lou, *CrystEngComm*, 2013, **15**, 9332; (*b*) P. Du, L. X. Song, J. Xia, Y. Teng and Z. K. Yang, *J. Mater. Chem. A*, 2014, **2**, 11439; (*c*) K. F. Chen, S. Y. Song and D. F. Xue, *CrystEngComm*, 2013,

15, 144; (*d*) F. Liu, S. Y. Song, D. F. Xue and H. J. Zhang, *Adv. Mater.*, 2012, **24**, 1089; (*e*) L. Zhang, G. Q. Zhang, H. B. Wu, L. Yu and X. W. Lou, *Adv. Mater.*, 2013, **25**, 2589.

37 N. Sharma, K. M. Shaju, G. V. S. Rao, B. V. R. Chowdari, Z. L. Dong and T. J. White, *Chem. Mater.*, 2004, **16**, 504.

38 N. N. Leyzerovich, K. G. Bramnik, T. Buhrmester, H. Ehrenberg and H. Fuess, *J. Power Sources*, 2004, **127**, 76.

39 W. Xiao, J. S. Chen, C. M. Li, R. Xu and X. W. Lou, *Chem. Mater.*, 2010, **22**, 746.

40 (*a*) D. H. Wei, J. W. Liang, Y. C. Zhu, J. J. Zhang, X. N. Li, K. L. Zhang, Z. Q. Yuan and Y. T. Qian, *Electrochim. Acta*, 2013, **114**, 779; (*b*) X. Q. Liu and I. Willner, *Adv. Mater.*, 2013, **25**, 349; (*c*) W. Wang, Y. Xiao, X. Y. Zhao, B. Liu and M. H. Cao, *CrystEngComm*, 2014, **16**, 922.